Journal of the Mechanical Behavior of Biomedical Materials 86 (2018) 409–422

Contents lists available at ScienceDirect

Journal of the Mechanical Behavior of Biomedical Materials

journal homepage: www.elsevier.com/locate/jmbbm

On incorporating osmotic prestretch/prestress in image-driven finite element simulations of cartilage

Xiaogang Wang[a], Thomas S.E. Eriksson[b], Tim Ricken[c], David M. Pierce[a,d,*]

[a] Department of Mechanical Engineering, University of Connecticut, Storrs, CT, USA
[b] Department of Defense and Security, System and Technology, Weapons and Protection, FOI – Swedish Defense Research Agency, Stockholm, Sweden
[c] Institute for Mechanics, Structural Analysis and Dynamics, Stuttgart University, Stuttgart, Germany
[d] Department of Biomedical Engineering, University of Connecticut, Storrs, CT, USA

ARTICLE INFO

Keywords:
Cartilage
Osmotic pressure
Finite element analysis
Constitutive modeling
Backward displacement method
Medical imaging

ABSTRACT

Medical imaging performed *in vivo* captures geometries under Donnan osmotic loading, even when the articulating joint is otherwise mechanically unloaded. Hence patient-specific finite element (FE) models constructed from such medical images of cartilage represent osmotically induced prestretched/prestressed states. When applying classical modeling approaches to patient-specific simulations of cartilage a theoretical inconsistency arises: the *in-vivo* imaged geometry (used to construct the model) is not an unloaded, stress-free reference configuration. Furthermore when fitting nonlinear constitutive models that include osmotic swelling (to obtain material parameters), if one assumes that experimental data–generated from osmotically loaded cartilage–begin from a stress-free reference configuration the fitted stress-stretch relationship (parameters) obtained will actually describe a different behavior. In this study we: (1) establish a practical computational method to include osmotically induced prestretch/prestress in image-driven simulations of cartilage; and (2) investigate the influence of considering the prestretched/prestressed state both when fitting fiber-reinforced, biphasic constitutive models of cartilage that include osmotic swelling and when simulating cartilage responses. Our results highlight the importance of determining the prestretched/prestressed state within cartilage induced by osmotic loading in the imaged configuration prior to solving boundary value problems of interest. With our new constitutive model and modeling methods, we aim to improve the fidelity of FE-based, patient-specific biomechanical simulations of joints and cartilage. Improved simulations can provide medical researchers with new information often unavailable in a clinical setting, information that may contribute to better insight into the pathophysiology of cartilage diseases.

1. Introduction

Magnetic resonance imaging (MRI) is currently the most important tool to assess pathologic changes in knee cartilage, in both clinical and research environments, and its prevalence is increasing (Crema et al., 2011). Such imaging is performed *in vivo*, hence finite element (FE) models constructed from medical images of cartilage represent geometries under Donnan osmotic loading even when the articulating joint is otherwise mechanically unloaded. Osmotic pressure develops as fluid is chemically driven into cartilage because the total ion concentration within the tissue is greater than that within the joint (or external bathing solution), and this continues until it is balanced by a mechanical counter pressure. This osmotically induced stretch/stress exists prior to constructing the image-driven geometry of the model, and thus we refer to it as a prestretched/prestressed state. Yet, classical continuum mechanics and FE analyses generally assume that constitutive models and the corresponding simulations start from undeformed/unloaded, stress-free reference configurations. Thus, when applying classical modeling approaches to patient-specific simulations of cartilage a theoretical inconsistency arises: the *in-vivo* imaged geometry (used to construct the model) is not an unloaded, stress-free reference configuration.

Furthermore, most mechanical experiments on cartilage start from this osmotically swollen condition such that the initial osmotic pressure generates a prestressed solid matrix accompanied by a compatible volumetric deformation (Karajan, 2009). Cartilage specimens, when removed from the joint and placed into a physiological bathing solution, are commonly in this equilibrium state, and thus mechanical testing

* Corresponding author at: Departments of Mechanical Engineering and Biomedical Engineering, University of Connecticut, 191 Auditorium Road, Unit 3139, Storrs, CT 06269-3139, USA.
E-mail address: dmpierce@engr.uconn.edu (D.M. Pierce).

https://doi.org/10.1016/j.jmbbm.2018.06.014
Received 18 December 2017; Received in revised form 20 April 2018; Accepted 7 June 2018
Available online 15 June 2018
1751-6161/

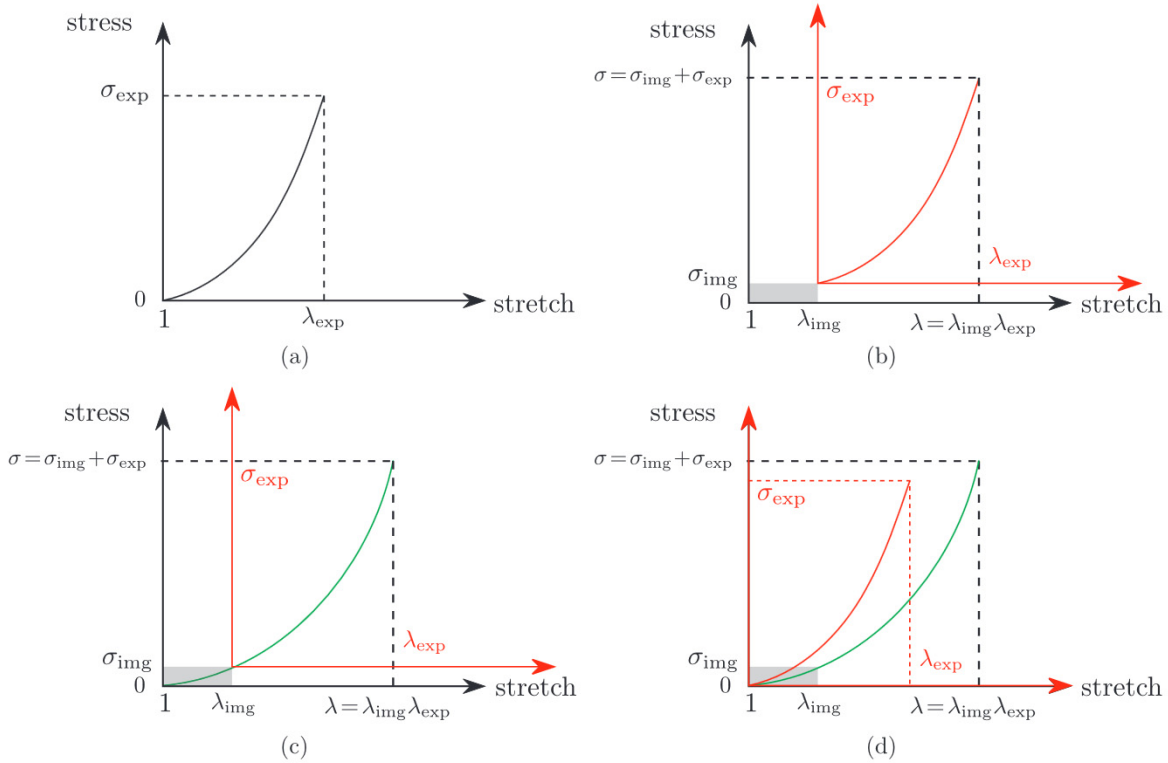

Fig. 1. Conceptual illustration of the effects of osmotic prestretch/prestress for a uniaxial tension test of a cartilage specimen in physiological solution. (a) Experimentally determined stress-stretch ($\sigma_{exp} - \lambda_{exp}$) response where we assume an initial stress-free reference configuration for the specimen, i.e. no prestretch. (b) Experimentally determined stress-stretch response where we include an initial osmotically swollen prestretched-prestressed ($\sigma_{img} - \lambda_{img}$) configuration for the specimen referenced to the (unknown) stress-free reference configuration. (c) The (unknown) true stress-stretch diagram (the green curve) of the specimen, including the osmotic prestretch/prestress. (d) A simulation naively fitted directly to experimentally determined stress-stretch data (red) in (a) fails to reproduce the correct result (green).

commonly occurs on prestretched/prestressed specimens (often assumed to have no initial deformation). If one assumes that the resulting experimental data begin from a stress-free reference configuration when fitting nonlinear constitutive models that include osmotic swelling (to obtain material parameters) the fitted stress-stretch relationship (parameters) obtained will actually describe a different behavior. Fig. 1, using a uniaxial tension test as representative example, clarifies the effects of osmotic prestretch/prestress in interpreting mechanical data, cf. (Karajan, 2009).

1.1. Background

Articular cartilage comprises, by percentage wet weight, heterogeneously distributed fluid and electrolytes (68–85%), collagen fibers (15–25%), proteoglycans (5–10%) and chondrocytes (<4%) (Mow et al., 2005). The heterogeneous solid phase constitutes a negatively charged proteoglycan (PG) mesh and a fiber network of predominantly type II collagen, both of which contribute to mechanical stiffness and permeation of the fluid. Densely packed and negatively charged PGs increase in concentration from the articulating surface to subchondral bone (Mow et al., 2005; Mansour, 2008; Pierce et al., 2016). There are generally three sub-tissue zones through the thickness (from the surface to the subchondral bone): fibers are predominantly tangential to the articular surface in the superficial zone; become isotropically distributed and oriented in the middle zone; and are predominantly perpendicular to the underlying bone in the deep zone (Mow et al., 2005). The remarkable macro-mechanics of cartilage derive from the complex micro-mechanics of proteoglycans, collagens, and electrolytic fluid interacting (Broom and Marra, 1986; Zhu et al., 1993).

Negative charges associated with the PGs, known as the fixed charge density (FCD) in articular cartilage, draw in surrounding synovial fluid to generate osmotic pressure, which results primarily from Donnan and entropic effects (Chahine et al., 2005). However, Donnan osmotic pressure contributes over 85% of the total measured swelling pressure (Urban and Maroudas, 1981). The tissue imbibes fluid until the mechanical counter pressure resulting from greater fluid volume within the tissue equals the chemically driven movement of the fluid (to dilute the solution). Cartilage comes to equilibrium *in vivo* when the intratissue solid stresses balance the osmotic pressure. Such swelling prestretches the network of collagen fibers (Setton et al., 1998) and may significantly affect the mechanics of cartilage.

Numerical analyses of joints and cartilage can provide medical researchers with new information often unavailable in a clinical setting, information that may contribute to better insight into the pathophysiology of cartilage diseases, e.g. osteoarthritis. Numerical analyses also offer a flexible, cost-effective, and patient-friendly environment in which both new and existing medical treatments can be tested and optimized. FE models are already widely used to study the mechanical responses of joints and cartilage, and the properties of cartilage (Klika et al., 2016). With the continuous improvement of computational methods and power, and medical imaging, numerical analyses, e.g. FE models, will eventually be used in clinical practice, with a trend toward more realistic patient-specific models. Image-driven, patient-specific simulations, in conjunction with multiphase (poroelastic) constitutive models calibrated and validated with experimental data can model and predict realistic responses of cartilage.

Prior studies in 3-D include the effects of osmotic pressure, e.g.: van Loon et al. (2003), Chen et al. (2006), Schroeder et al. (2006), Ehlers et al. (2009), Ateshian et al. (2009), Ehlers et al. (2010), Ateshian et al. (2011), however the influences of prestretch/stress in the solid matrix, and specifically the network of collagen fibers, are rarely investigated. In one such paper, Ehlers et al. (2009) formulated a general constitutive

model applicable to almost any charged, hydrated tissue. Within the theory of porous media (TPM) they combined large-strain, Ogden-type material laws for the solid matrix with osmotic effects based on the simplifying assumption of Lanir (1987). In this contribution the authors described the osmotic properties without considering the ion concentrations (or electro-chemical potentials) as additional unknowns in the process. Instead, they split the solid extra stress into osmotic and mechanical contributions. While the authors applied their 3-D, large-strain framework to human intervertebral disc, we apply their model for osmotic pressure to articular cartilage.

Ateshian et al. (2009) modeled the solid matrix of cartilage with a continuous angular distribution of fibers, where fibers can only sustain tension, swelled by the osmotic pressure of a proteoglycan ground matrix. They particularized their constitutive model to focus on the tissue's equilibrium response to mechanical and osmotic loading, when flow-dependent and flow-independent viscoelastic effects subsided. The authors implemented this material model into a custom-written, 3-D FE code including finite deformation and investigated both the stress-stretch response and effective Poisson's ratio in simulations of compression and tension. Applying this model, they successfully predicted a number of observed phenomena in relation to the tissue's equilibrium response to mechanical and osmotic loading and demonstrated that anisotropy of the fibrillar matrix of articular cartilage is dependent on the mechanism of strain-dependent fiber recruitment.

1.2. Objectives

The objectives of this study are two-fold: (1) to establish a practical computational method to include osmotic pressure in image-driven simulations of cartilage; and (2) to investigate (by application of the new methods) the influence of considering the prestretched/prestressed state both when fitting fiber-reinforced, biphasic constitutive models of cartilage that include osmotic swelling and when simulating cartilage responses. Towards objective (1) we extend our recent constitutive model for cartilage (Pierce et al., 2016) to include the mechanical effects of osmotic pressure (following Karajan, 2009; Ehlers et al., 2009), and determine the prestretched/prestressed state within the solid matrix induced by osmotic loading in the (imaged) initial configuration of the FE model using the backward displacement method (following Bols et al., 2013) prior to solving boundary value problems of interest. Further, we compare results from simulations with/without including osmotic contributions. Towards objective (2) we fit our new constitutive model for cartilage with/without considering osmotic contributions and considering different initial configurations, and compare the resulting stress-stretch responses and parameters. Finally, we compare results from image-driven simulations based on measured Diffusion Tensor Magnetic Resonance Images (DT-MRI) both with/without including osmotic contributions and considering different initial configurations.

2. Methods

2.1. Constitutive model for cartilage

We extend our image-driven constitutive model for cartilage (Pierce et al., 2016, 2018), and corresponding 3-D nonlinear FE implementation, to include the mechanical effects of osmotic pressure. During normal movement cartilage undergoes large deformations *in vivo* (compressing greater than 20% under pressures up to 20 MPa Park et al., 2003; Mow et al., 2005; Bingham et al., 2008; Liu et al., 2010; Chan et al., 2016), hence we employ large-strain kinematics and nonlinear mechanics. To this end, we selected the biphasic swelling approach of Ehlers et al. (2009) wherein we do not solve for the concentration fields of the solutes, cf. Karajan (2009) for further details. Therein the osmotic pressure, which is usually associated with the interstitial pore fluid, is computed from the solid strain energy since the FCD is immobilized within the ECM (Wilson et al., 2005). Furthermore, we assume(1) *a priori* chemical equilibrium due to the innate (long-established) natural ion distribution, (2) large disturbances are unlikely *in vivo*, and (3) negligible electrochemical potential (i.e. electro-neutrality) due to much faster diffusion of small ions relative to bulk fluid permeation (Lanir, 1987; Karajan, 2009; Ehlers et al., 2009).

Briefly, we use the theory of porous media to describe articular cartilage as a biphasic swelling continuum $\varphi = \varphi^{\mathrm{S}} + \varphi^{\mathrm{F}}$ which consists of a porous solid phase φ^{S} saturated with the interstitial fluid phase φ^{F} (Bowen, 1980, 1982; Ehlers, 1989, 1993; de Boer, 2000; Pence, 2012). The volume fractions n^{α} refer the volume elements $\mathrm{d}v^{\alpha}$ of the individual constituents φ^{α} to the bulk volume element $\mathrm{d}v$ with $n^{\alpha}(\mathbf{x}, t) = \mathrm{d}v^{\alpha}/\mathrm{d}v$, $\sum_{\alpha=1}^{k} n^{\alpha}(\mathbf{x}, t) = \sum_{\alpha=1}^{k} \rho^{\alpha}/\rho^{\alpha\mathrm{R}} = 1$, $\alpha \in \{\mathrm{S},\ \mathrm{F}\}$, where $\mathbf{x}$ is the position vector of the spatial point (reference position $\mathbf{X}$), t is the time, and S and F denote the solid and fluid, respectively. The partial density $\rho^{\alpha} = n^{\alpha}\,\rho^{\alpha\mathrm{R}}$ of the constituent φ^{α} is related to the real density of the materials $\rho^{\alpha\mathrm{R}}$ involved via the volume fractions n^{α}. We formulate the total Cauchy stress tensor as

$$\boldsymbol{\sigma} = -p\,\mathbf{I} + \boldsymbol{\sigma}_{\mathrm{E}}^{\mathrm{S}} = -p\,\mathbf{I} + 2\,\rho^{\mathrm{S}}\,\mathbf{F}_{\mathrm{S}}\frac{\partial \Psi^{\mathrm{S}}}{\partial \mathbf{C}_{\mathrm{S}}}\,\mathbf{F}_{\mathrm{S}}^{\mathrm{T}}, \tag{1}$$

where p is the fluid pore pressure, $\boldsymbol{\sigma}_{\mathrm{E}}^{\mathrm{S}}$ is the effective Cauchy stress tensor (Bishop, 1959; Skempton, 1960), $\mathbf{I}$ is the identity tensor, $\mathbf{F}_{\mathrm{S}} = \partial \mathbf{x}_{\mathrm{S}}/\partial \mathbf{X}_{\mathrm{S}}$ is the deformation gradient of the solid, and $\mathbf{C}_{\mathrm{S}} = \mathbf{F}_{\mathrm{S}}^{\mathrm{T}}\,\mathbf{F}_{\mathrm{S}}$ is the right Cauchy-Green tensor. We use an additive decomposition of the superimposed solid Helmholtz free-energy function Ψ^{S} into a Donnan osmotic pressure part $\Psi_{\mathrm{OP}}^{\mathrm{S}}$, an isotropic matrix part $\Psi_{\mathrm{IM}}^{\mathrm{S}}$, and a fiber network part $\Psi_{\mathrm{FN}}^{\mathrm{S}}$ as

$$\Psi^{\mathrm{S}} = \Psi_{\mathrm{OP}}^{\mathrm{S}}(J_{\mathrm{S}}) + (1-\nu)\Psi_{\mathrm{IM}}^{\mathrm{S}}(J_{\mathrm{S}},\ I_1) + \nu\Psi_{\mathrm{FN}}^{\mathrm{S}}(\mathbf{C}_{\mathrm{S}}), \tag{2}$$

where ν is the volume fraction of collagen to the total solid, $J_{\mathrm{S}} = \det \mathbf{F}_{\mathrm{S}}$ is the Jacobian and $I_1 = \mathrm{tr}\mathbf{C}_{\mathrm{S}}$ is the first invariant of $\mathbf{C}_{\mathrm{S}}$.

Donnan osmotic pressure arises as negatively charged PG (specifically glycosaminoglycan or GAG chains), enmeshed within the collagen network, interact with electrolytes in the interstitial fluid to swell the tissue. We define the molar concentrations of dissolved ions and fixed charges as $c_{\mathrm{m}}^{\gamma} := \mathrm{d}N^{\gamma}/\mathrm{d}v^{\mathrm{F}}$, with $\gamma = \{+,-,\mathrm{fc}\}$, where $\bar{c}_{\mathrm{m}}^{-} = \bar{c}_{\mathrm{m}}^{+} =: \bar{c}_{\mathrm{m}}$ is the ion concentration of the external solution (here treated as a material parameter and not a boundary condition), $c_{\mathrm{m}}^{-} = c_{\mathrm{m}}^{+} - c_{\mathrm{m}}^{\mathrm{fc}}$ corresponds to the internal solution. Furthermore, the concentration of the fixed charges depends on the deformation, i.e.

$$\begin{aligned} c_{\mathrm{m}}^{\mathrm{fc}} &= c_{0\mathrm{S}}^{\mathrm{fc}}\,n_{0\mathrm{S}}^{\mathrm{F}}(\det \mathbf{F}_{\mathrm{S}} - n_{0\mathrm{S}}^{\mathrm{S}})^{-1} \\ &= c_{0\mathrm{S}}^{\mathrm{fc}}(1-n_{0\mathrm{S}}^{\mathrm{S}})(\det \mathbf{F}_{\mathrm{S}} - n_{0\mathrm{S}}^{\mathrm{S}})^{-1}, \end{aligned} \tag{3}$$

where $n_{0\mathrm{S}}^{\alpha}$ are initial volume fractions and $c_{0\mathrm{S}}^{\mathrm{fc}}$ is the initial concentration of fixed charges within the tissue. Thus, we capture the osmotic strain energy as (Karajan, 2009; Ehlers et al., 2009)

$$\Psi_{\mathrm{OP}}^{\mathrm{S}} = R\,\Theta\,c_{0\mathrm{S}}^{\mathrm{fc}}\,n_{0\mathrm{S}}^{\mathrm{F}}\left[\frac{2\bar{c}_{\mathrm{m}}}{c_{\mathrm{m}}^{\mathrm{fc}}} - \frac{\sqrt{4(\bar{c}_{\mathrm{m}})^2 + (c_{\mathrm{m}}^{\mathrm{fc}})^2}}{c_{\mathrm{m}}^{\mathrm{fc}}} + \mathrm{asinh}\left(\frac{c_{\mathrm{m}}^{\mathrm{fc}}}{2\bar{c}_{\mathrm{m}}}\right)\right], \tag{4}$$

where $R = 8.314(\mathrm{MPa\ mm^3})/(\mathrm{K\ mol})$ is the universal gas constant and Θ is the absolute temperature (details in Appendix A).

We capture the strain energy of the (largely) proteoglycan solid matrix using a neoHookean strain-energy function for $\Psi_{\mathrm{IM}}^{\mathrm{S}}$ (Simo and Pister, 1984), which we extend to include compaction effects as (Bluhm, 2002; Pierce et al., 2013a, 2013b, 2016)

$$\Psi_{\mathrm{IM}}^{\mathrm{S}}(J_{\mathrm{S}},\ I_1) = \frac{1}{\rho_{0\mathrm{S}}^{\mathrm{S}}}\left[U(J_{\mathrm{S}}) + \frac{1}{2}\,\mu^{\mathrm{S}}(I_1-3)\right], \tag{5}$$

where

$$U(J_{\mathrm{S}}) = \chi_{\mathrm{cp}}^{\mathrm{S}}\left[\frac{1}{2}(\log J_{\mathrm{S}})^2 + \zeta^{\mathrm{S}}\right] - \mu^{\mathrm{S}}\log J_{\mathrm{S}}, \tag{6}$$

and where we use the abbreviations

$$\chi^{\mathrm{S}}_{\mathrm{cp}} = \lambda^{\mathrm{S}}\left[1 + J^{\mathrm{S}}_{\mathrm{cp}}\left(1 + \frac{(J^{\mathrm{S}}_{\mathrm{cp}})^2}{1 - J^{\mathrm{S}}_{\mathrm{cp}}}\right)\right]^{-1},$$
$$\zeta^{\mathrm{S}} = J^{\mathrm{S}}_{\mathrm{cp}} \log J_{\mathrm{S}} + \frac{1 - J^{\mathrm{S}}_{\mathrm{cp}}}{J^{\mathrm{S}}_{\mathrm{cp}} - 2} \left[\log \frac{J^{\mathrm{S}}_{\mathrm{cp}} - J_{\mathrm{S}}}{J_{\mathrm{S}}(J^{\mathrm{S}}_{\mathrm{cp}} - 1) - J^{\mathrm{S}}_{\mathrm{cp}}} - \log(1 - J^{\mathrm{S}}_{\mathrm{cp}})\right]. \tag{7}$$

In (5)–(7) μ^{S} is Lamé's second parameter (corresponding to the shear modulus of the underlying matrix in the reference configuration), λ^{S} is Lamé's first parameter (which degenerates to a non-physical, penalty parameter used to enforce incompressibility, cf. Pence, 2012), and $n^{\mathrm{S}}_{0\mathrm{S}} \le J^{\mathrm{S}}_{\mathrm{cp}} \le 1$ defines the point of compaction for the tissue, where $n^{\mathrm{S}}_{0\mathrm{S}}$ is the solid volume fraction in the reference configuration and it is generally not possible to 'squeeze out' all of the fluid from the tissue.

To capture the anisotropic, nonlinear response of the dispersed network of collagen, let $\rho(\mathbf{M})$ be the angular density of fibers (the Orientation Distribution Function or ODF) so that (Miehe et al., 2004; Lei and Szeri, 2006)

$$\frac{1}{4\pi}\int_{\Omega} \rho(\mathbf{M})\mathrm{d}\Omega = 1, \tag{8}$$

where $\Omega = \mathbf{M} \in \mathbb{R}^3$: $|\mathbf{M}| = 1$ is the unit sphere. For a single fiber of reference orientation $\mathbf{M}$ the fourth pseudo-invariant I_4 is the square of the stretch of this fiber in the direction $\mathbf{m} = \mathbf{F}_{\mathrm{S}}\mathbf{M}$, i.e. $I_4(\mathbf{M}) = \lambda^2(\mathbf{M}) = \mathbf{M}\cdot\mathbf{C}_{\mathrm{S}}\mathbf{M}$. We capture the strain energy of the dispersed collagen network as

$$\Psi_{\mathrm{FN}}(\mathbf{C}, \mathbf{M}) = \frac{1}{\rho^{\mathrm{S}}_{0\mathrm{S}}}\int_{\Omega} \rho(\mathbf{M})\frac{k_1}{2k_2}\{\exp[k_2(I_4 - 1)^2] - 1\}\mathscr{H}(I_4 - 1)\mathrm{d}\Omega, \tag{9}$$

where $k_1 > 0$ is a material parameter, $k_2 > 0$ is a dimensionless parameter and $\mathscr{H}$ is a Heaviside step function evaluated at $(I_4 - 1)$, i.e. collagen fibers engage only under $\lambda > 1$ (Holzapfel et al., 2000).

To model the corresponding permeation of interstitial fluid, we introduce the seepage velocity $\mathbf{w}_{\mathrm{FS}}$, which describes the difference in velocity between the fluid phase $\mathbf{x}'_{\mathrm{F}}$ and the solid phase $\mathbf{x}'_{\mathrm{S}}$ as $\mathbf{w}_{\mathrm{FS}} = \mathbf{x}'_{\mathrm{F}} - \mathbf{x}'_{\mathrm{S}}$. We determine the filtration velocity $n^{\mathrm{F}}\mathbf{w}_{\mathrm{FS}}$ as $n^{\mathrm{F}}\mathbf{w}_{\mathrm{FS}} = \mathbf{K}_{\mathrm{F}}(-\mathrm{grad}\, p + \rho^{\mathrm{FR}}\mathbf{b})$, where $\mathbf{K}_{\mathrm{F}}$ is the anisotropic intrinsic permeability of the cartilage solid matrix and $\mathbf{b}$ is the body force per unit mass (Pierce et al., 2016). Since permeation of interstitial fluid is least restricted in the direction parallel to the fibers (Filidoro et al., 2005; Meder et al., 2006; Abdullah et al., 2007; de Visser et al., 2008a, 2008b) we define $\mathbf{K}_{\mathrm{F}}$ as (Ricken and Bluhm, 2010; Pierce et al., 2016)

$$\mathbf{K}_{\mathrm{F}} = \frac{k_{0\mathrm{S}}}{4\pi}\left(\frac{n^{\mathrm{F}}}{1 - n^{\mathrm{S}}_{0\mathrm{S}}}\right)^m \int_{\Omega} \frac{\rho(\mathbf{M})}{I_4(\mathbf{m})}\mathbf{m}\otimes\mathbf{m}\,\mathrm{d}\Omega, \tag{10}$$

where $k_{0\mathrm{S}}$ [m^4/Ns] is the initial Darcy permeability and m is a dimensionless parameter controlling the general isotropic deformation dependence of the permeability (Eipper, 1998).

To facilitate image-based, patient-specific modeling, we may determine the local microstructure of collagen fibers, i.e. the ODF required in (9) and (10), directly from, e.g. diffusion-tensor MRI, as

$$\rho(\mathbf{M}, \mathbf{D}) = \frac{\sin\theta}{|\mathbf{D}|^{1/2}(\mathbf{M}^{\mathrm{T}}\mathbf{D}^{-1}\mathbf{M})^{3/2}}, \tag{11}$$

where $(\mathbf{M}) = (\cos\theta\sin\phi,\ \sin\theta\sin\phi,\ \cos\phi)^{\mathrm{T}}$ and $\mathbf{D}$ is the experimentally determined diffusion tensor.

2.2. Backward displacement method

It is generally not possible to measure a true stress-free reference configuration *in vivo*. Using the backward displacement method (following Bols et al., 2013) we define and solve an inverse problem to determine the *in vivo* prestretch/prestress distribution in equilibrium with the imaged configuration, without the need of an imaginary stress-free reference configuration.

We begin by defining a general forward problem. We start our analysis from a stress-free reference configuration $\mathcal{B}_0(\mathbf{X}, \mathbf{0})$, where $\mathbf{X}$ are the material coordinates of the undeformed reference geometry and the second argument refers to the unloaded stress state in this configuration. A forward analysis then determines a swelled *in-vivo* equilibrium state (coincident with the imaged configuration) $\mathcal{B}_{\mathrm{img}}(\mathbf{x}_{\mathrm{img}}, \boldsymbol{\sigma}_{\mathrm{img}})$, where $\mathbf{x}_{\mathrm{img}}$ are the coordinates of the swelled geometry and $\boldsymbol{\sigma}_{\mathrm{img}}$ is the corresponding stress state. This imaged configuration results from a prescribed load, which here we take as the osmotic pressure $\Delta\pi$. Specifically, we have (cf. (3) and Appendix A)

$$\Delta\pi = \Delta\pi(n^{\mathrm{S}}_{0\mathrm{S}}, c^{\mathrm{fc}}_{0\mathrm{S}}, \det\mathbf{F}_{\mathrm{S}}). \tag{12}$$

At the stress-free reference configuration $\mathcal{B}_0$, $\det\mathbf{F}_{\mathrm{S}} = 1$, and thus for the initial osmotic pressure $\Delta\pi_0$ we have

$$\Delta\pi_0 = \Delta\pi_0(n^{\mathrm{S}}_{0\mathrm{S}}, c^{\mathrm{fc}}_{0\mathrm{S}}, 1). \tag{13}$$

N.B. naturally $\Delta\pi_0 = 0$ when $c^{\mathrm{fc}}_{0\mathrm{S}} = 0$, so that no osmotic pressure exists if there is no FCD. We can now solve this forward problem, given the initial reference geometry and parameters for the osmotic pressure, to determine the osmotically swelled equilibrium configuration Γ with both geometry (stretch) and stress information. We the concisely define the solution process as

$$\mathcal{B}_{\mathrm{img}}(\mathbf{x}_{\mathrm{img}}, \boldsymbol{\sigma}_{\mathrm{img}}) = \Gamma(\mathcal{B}_0(\mathbf{X}, \mathbf{0}), \Delta\pi_0(n^{\mathrm{S}}_{0\mathrm{S}}, c^{\mathrm{fc}}_{0\mathrm{S}}, 1)) = \Gamma(\mathcal{B}_0, \Delta\pi_0). \tag{14}$$

In the backward problem, the stress-free reference configuration and the stress state in equilibrium with the imaged (*in-vivo*) configuration are unknown (denoted with superscript U, i.e. $\square^{\mathrm{U}}$),

$$\mathbf{X} = \mathbf{X}^{\mathrm{U}},\ \ \boldsymbol{\sigma}_{\mathrm{img}} = \boldsymbol{\sigma}^{\mathrm{U}}_{\mathrm{img}}, \tag{15}$$

while the imaged configuration and the input parameters for the initial osmotic pressure are known (denoted with superscript K, i.e. $\square^{\mathrm{K}}$),

$$\mathbf{x} = \mathbf{x}^{\mathrm{K}}_{\mathrm{img}},\ \ \Delta\pi_0 = \Delta\pi^{\mathrm{K}}_0. \tag{16}$$

We can now rewrite the backward problem as a forward analysis,

$$\mathcal{B}_{\mathrm{img}}(\mathbf{x}^{\mathrm{K}}_{\mathrm{img}}, \boldsymbol{\sigma}^{\mathrm{U}}_{\mathrm{img}}) = \Gamma(\mathcal{B}_0(\mathbf{X}^{\mathrm{U}}, \mathbf{0}), \Delta\pi^{\mathrm{K}}_0), \tag{17}$$

resulting in the stress field $\boldsymbol{\sigma}^{\mathrm{U}}_{\mathrm{img}}$ defined as the desired, prestressed state. For clarity, we formulate the inverse problem: given the configuration $\mathbf{x}^{\mathrm{K}}_{\mathrm{img}}$ imaged *in vivo* and the prescribed osmotic pressure $\Delta\pi^{\mathrm{K}}_0$, determine the corresponding stress state $\boldsymbol{\sigma}^{\mathrm{U}}_{\mathrm{img}}$ creating mechanical equilibrium in the configuration $\mathcal{B}_{\mathrm{img}}(\mathbf{x}^{\mathrm{K}}_{\mathrm{img}}, \boldsymbol{\sigma}^{\mathrm{U}}_{\mathrm{img}})$.

To solve this problem, we extend the iterative fixed point algorithm of Bols et al. (2013) and utilize a forward FE solver (detailed in Algorithm 1). Each iteration i starts with a guess of the (imaginary) stress-free configuration $\mathbf{X}^{(i)}$, and for the first iteration ($i = 1$) we use the imaged geometry as the first guess ($\mathbf{X}^{(1)} = \mathbf{x}^{\mathrm{K}}_{\mathrm{img}}$). From our guess, and the given osmotic load $\Delta\pi^{\mathrm{K}}_0$, a forward solver determines the corresponding equilibrium configuration $\mathcal{B}^{(i)}_{\mathrm{img}}(\mathbf{x}^{(i)}_{\mathrm{img}}, \boldsymbol{\sigma}^{(i)}_{\mathrm{img}}) = \Gamma(\mathcal{B}_0(\mathbf{X}^{(i)}, \mathbf{0}), \Delta\pi^{\mathrm{K}}_0)$. We then calculate a residual characterizing the difference between the current equilibrium and the desired (imaged) configurations. We define the residual of the jth node in the ith iteration's equilibrium configuration $\mathbf{x}^{(i)}_{\mathrm{img},j}$ as

$$r^{(i)}_j = \| \mathbf{x}^{\mathrm{K}}_{\mathrm{img},j} - \mathbf{x}^{(i)}_{\mathrm{img},j} \|,\ \forall\, j \in [1, N_{\mathrm{node}}], \tag{18}$$

where $\|\square\|$ is the L^2-norm and N_{node} is the total number of nodes in the FE model. We achieve convergence when the maximum residual among

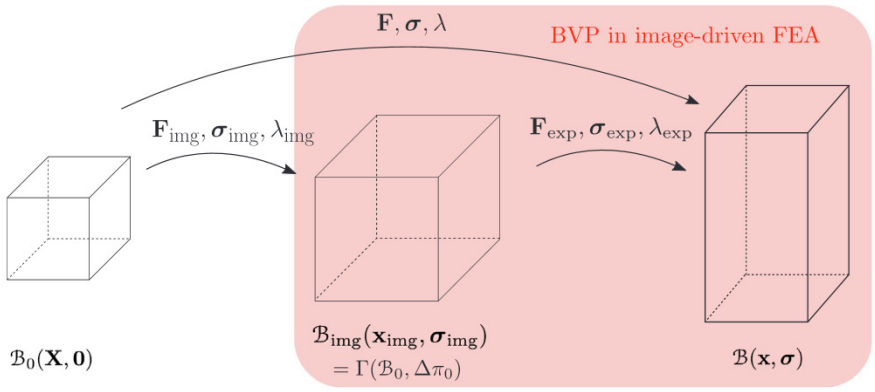

Fig. 2. Conceptual illustration of the relevant configurations for mechanical analyses. Configuration $\mathcal{B}_0$ is an (imaginary) stress-free reference configuration. By application of osmotic loading (and a regular forward analysis) we swell to the corresponding imaged configuration $\mathcal{B}_{\text{img}}$ in equilibrium with the osmotic pressure. By application of additional loads, e.g. a specific experimental condition, we further deform to the current configuration $\mathcal{B}$. In solving boundary value problems (BVP) in image-driven FE of cartilage we are only concerned with analyses from the imaged configuration $\mathcal{B}_{\text{img}}$ to the current configuration $\mathcal{B}$ (red box).

all nodes is below the convergence criterion ϵ, i.e.

$$r^{(i)}_{\max} = \max_{j\in[1,N_{\text{nodel}}]} \{r^{(i)}_j\} < \epsilon. \tag{19}$$

If convergence is not reached, we use the displacement

$$\mathbf{U}^{(i)}_{\text{img}} = \mathbf{x}^{(i)}_{\text{img}} - \mathbf{X}^{(i)}, \tag{20}$$

to update our guess of the (imaginary) stress-free configuration as $(\mathbf{x}^{\text{K}} - \mathbf{U}^{(i)}_{\text{img}})$. We introduce a step size $\xi > 0$ to control the efficiency and robustness by controlling the interpolation between the current (approximate) $\mathbf{X}^{(i)}$ and the updated approximation $(\mathbf{x}^{\text{K}} - \mathbf{U}^{(i)}_{\text{img}})$. Thus, the new guess $\mathbf{X}^{(i+1)}$ is

$$\mathbf{X}^{(i+1)} = \xi(\mathbf{x}^{\text{K}} - \mathbf{U}^{(i)}_{\text{img}}) + (1-\xi)\mathbf{X}^{(i)}. \tag{21}$$

When $\xi = 1$ we recover the method of Bols et al. (2013), i.e. $\mathbf{X}^{(i+1)} = (\mathbf{x}^{\text{K}} - \mathbf{U}^{(i)}_{\text{img}})$. Once we reach convergence, (17) is satisfied with $\mathbf{X}^{\text{U}} = \mathbf{X}^{(i)}$ and $\boldsymbol{\sigma}^{\text{U}}_{\text{img}} = \boldsymbol{\sigma}^{(i)}$.

Algorithm 1. Algorithm to recover the prestretched/prestressed state corresponding to the *in-vivo* imaged configuration.

$i \leftarrow 0$ ▷ initializing
$\mathbf{X}^{(1)} \leftarrow \mathbf{x}^{\text{K}}_{\text{img}}$
while $i = 0$ or $r^{(i)}_{\max} \geq \epsilon$ **do**
  $i = i + 1$
  $\mathcal{B}_{\text{img}}(\mathbf{x}^{(i)}_{\text{img}}, \boldsymbol{\sigma}^{(i)}_{\text{img}}) = \Gamma(\mathcal{B}_0(\mathbf{X}^{(i)}, \mathbf{0}), \Delta\pi^{\text{K}}_0)$
  $\mathbf{U}^{(i)}_{\text{img}} = \mathbf{x}^{(i)}_{\text{img}} - \mathbf{X}^{(i)}$
  $\mathbf{X}^{(i+1)} = \xi(\mathbf{x}^{\text{K}} - \mathbf{U}^{(i)}_{\text{img}}) + (1-\xi)\mathbf{X}^{(i)}$ ▷ update
end while
$\mathbf{X}^{\text{U}} \leftarrow \mathbf{X}^{(i)}$
$\boldsymbol{\sigma}^{\text{U}}_{\text{img}} \leftarrow \boldsymbol{\sigma}^{(i)}$

In simulations of cartilage (or other soft tissues) initiated from geometries imaged *in vivo*, we do not require the 'unloaded' reference configuration ($\mathcal{B}_0$ in Fig. 2), but only that the intra-tissue stress distribution is in equilibrium with the known boundary conditions as imaged, such that simulations can begin from this equilibrium state ($\mathcal{B}_{\text{img}}$ in Fig. 2).

Table 1
The required material and structural parameters, the values used to approximate the response of cartilage from the middle zone, and the corresponding units.

Parameter	Value	Unit
ρ^{FR}	9.9×10^{-10}	ton/mm^3
ρ^{SR}	1.5×10^{-9}	ton/mm^3
μ^{S}	0.23	MPa
k_1	3.0	MPa
k_2	8.0	–
$n^{\text{S}}_{0\text{S}}$	0.21	–
ν	0.67	–
J^{S}_{cp}	0.41	–
$c^{\text{fc}}_{0\text{S}}$	2.0×10^{-7}	mol/mm^3
$\bar{c}_{\text{m}}$	1.5×10^{-7}	mol/mm^3
$k_{0\text{S}}$	6.2×10^{-4}	mm^4/(N s)
m	5.1	–
$\mathbf{D}$	(isotropic, see text)	–

2.3. Uniaxial extension test

To demonstrate our method and its impact, we first model a uniaxial tensile test of a cartilage specimen from the middle zone, consistent with the experiments completed in 0.15 M PBS bath by Elliott et al. (2002). Our FE model consists of a 1 mm × 1 mm × 1 mm cube meshed with a single 20-node hexahedral, Taylor-Hood element with quadratic

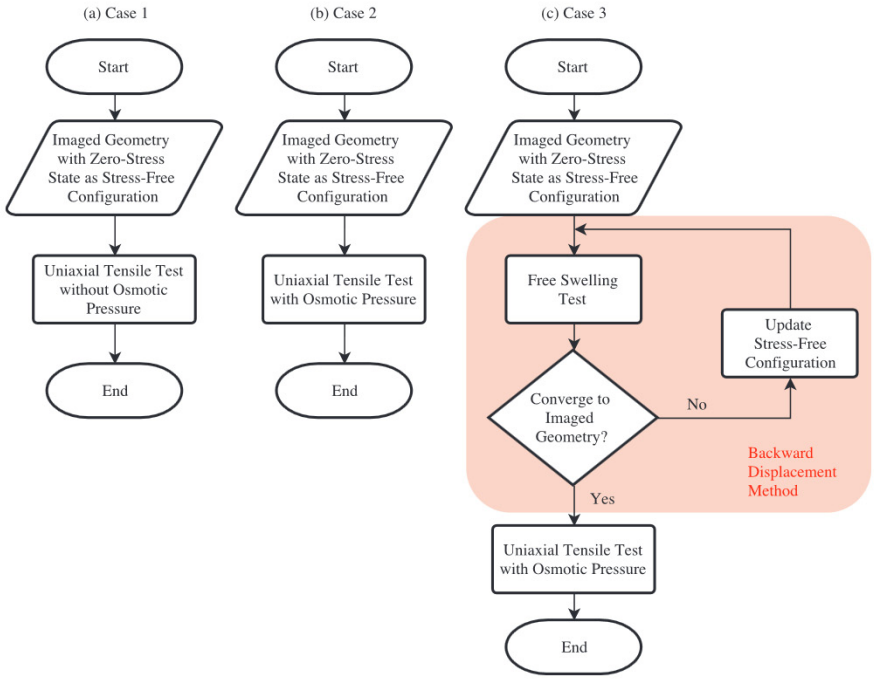

Fig. 3. Three different computational methods to simulate an (image-driven) uniaxial tension test. (a) Case 1 ignores the mechanical effects of osmotic pressure by setting the FCD to zero ($c_{0S}^{fc} = 0$), thus recovering the model of Pierce et al. (2016). (b) Case 2 naively accounts for osmotic pressure by treating the imaged configuration as a stress-free reference configuration. (c) Case 3 uses our new computational method to include osmotic pressure by first recovering the osmotically loaded prestressed state (red box), then simulating the uniaxial tensile test thereafter.

shape functions for solid displacements and bilinear shape functions for saturation pressure. We first fix nodes in dir-1, dir-2, and dir-3 at minimums to zero displacement in their respective directions. We then apply a linear displacement ramp to the nodes on one face of the cubic specimen (dir-1 equals maximum) at a quasi-static rate of 5×10^{-5} mm/s until we reach an applied stretch of 1.2 at 4000 s. Faces normal to the 2 and 3 directions (dir-2 and dir-3 equal maximum) are left free to expand or contract. We complete all simulations in the FE program FEAP (University of California at Berkeley, CA, USA) using a total Lagrangian formulation and the included Newton-Raphson algorithm.

Table 1 summarizes the material parameters we use to model human patellar cartilage from the middle zone, where we set $\beta_\alpha = 0$, $\tau_\alpha = 0.1$, $\alpha \in \{\text{IM, FN}\}$, to eliminate viscoelasticity in the solid constituents, cf. Pierce et al. (2016), and Θ= 310 K as the *in-vivo* temperature. We set the FCD c_{0S}^{fc} to that of healthy cartilage, cf. Räsänen et al. (2017). We set the DT-MRI tensor $[\mathbf{D}_{11}, \mathbf{D}_{22}, \mathbf{D}_{33}, \mathbf{D}_{12}, \mathbf{D}_{13}, \mathbf{D}_{23}] = [1.0, 1.0, 1.0, 5 \times 10^{-4}, 5 \times 10^{-4}, 5 \times 10^{-4}]$ to represent the isotropic distribution of the collagen fibers in the middle zone.

In light of the importance of this network of collagen fibers to the mechanical properties of articular cartilage, we treat the fiber parameters k_1 and k_2 carefully. In Section 2.3.1 we set $k_1 = 3.0$ MPa and $k_2 = 8.0$, cf. Pierce et al. (2013a), and compare results from simulations with/without including osmotic contributions and considering different initial configurations. In Section 2.3.2 we use $k_1 = 3.0$ MPa and $k_2 = 8.0$ as an initial reference, then fit our new constitutive model (Section 2.1) for cartilage to the experimental data from Elliott et al. (2002) with/without considering osmotic contributions and considering different initial configurations, and compare the resulting parameters.

To present our results and/or compare with the experimental results of Elliott et al. (2002) we clarify our stretch and stress measures. In the experimental data, both the experimentally determined stretches and stresses treat the imaged configuration as the reference configuration. Thus, the experimentally determined stretch λ_{exp} is

$$\lambda_{exp} = \frac{l}{l_{img}} = \frac{l}{l_0}\frac{l_0}{l_{img}} = \lambda\lambda_{img}^{-1}, \tag{22}$$

where l_0 is the relaxed dimension in the imaginary stress-free configuration, l_{img} is the corresponding dimension in the imaged configuration, and l is corresponding current length in deformed configuration. Similarly, the experimentally determined stress σ_{exp} is

$$\sigma_{exp} = \sigma - \sigma_{img}, \tag{23}$$

where σ and σ_{img} are defined in Section 2.2.

2.3.1. Comparing simulation methods

We use three different computational methods to simulate a uniaxial tension test, as detailed in Fig. 3. In Case 1 we turn off the mechanical effects of osmotic pressure by setting the FCD to zero ($c_{0S}^{fc} = 0$), thus recovering the model of Pierce et al. (2016). In Case 2 we naively account for osmotic pressure by treating the imaged configuration as a stress-free reference configuration. In Case 3 we apply our new computational method to include osmotic pressure by first recovering the (osmotically loaded) prestressed state using the backward displacement method, then simulating the uniaxial tensile test thereafter.

To illustrate the different predictions we plot Cauchy stress vs. experimentally determined stretch and quantify the percent differences in the predictions at $\lambda_{Ell} = 1.04, 1.08, 1.12$, i.e. following the experimental data of Elliott et al. (2002).

2.3.2. Fitting Model Parameters

To fit the material parameters k_1 and k_2 to the experimental data of Elliott et al. (2002) (while leaving all other parameters constant), we use a global design space (parameter range for fitting) in conjunction with parameter fitting using the three different computational methods to simulate the uniaxial tension test (Cases 1, 2, and 3; Fig. 3). Thus we have three combinations of fitted parameters that we then compare in light of the experimental data.

Our global design space encompasses virtually all reasonable possibilities with $k_1 \in [0, 10]$ (MPa), $k_2 \in (0, 15]$ (−). Within this range, we perform a nonlinear least-squares fitting to results generated from a

Fig. 4. We perform a nonlinear least-squares fitting to results generated from a two-step, optimization scheme. To reduce the computational cost we first employ a surrogate model (that can mimic the original response of the FE analysis) to determine a rough initial fitting (red box). Second, we use a gradient-based method to determine our final refined result (blue box) (For interpretation of the references to color in this figure legend, the reader is referred to the web version of this article).

Table 2
Through-thickness material, compositional, and structural parameters for cartilage and corresponding units (Pierce et al., 2016, Räsänen et al., 2017). The parameter $z^* \in [0, 1]$ is the normalized tissue thickness, where zero refers to the articular surface and one refers to the interface with subchondral bone.

Parameter	Value	Unit
$n_{0S}^{S}(z^*)$	$0.15 + 0.15(z^*)$	–
$\nu(z^*)$	$0.43(z^*)^2 - 0.60(z^*) + 0.85$	–
$J_{cp}^{S}(z^*)$	$0.36 + 0.11(z^*)$	–
$c_{0S}^{fc}(z^*)$	$[1.0 + 2.6(z^*)] \times 10^{-7}$, $z^* \in [0, 0.5]$	mol/mm^3
	2.3×10^{-7}, $z^* \in (0.5, 0.75]$	
	$[4.4 - 2.8(z^*)] \times 10^{-7}$, $z^* \in (0.75, 1]$	
$k_{0S}(z^*)$	$1.0 \times 10^{-3} - 0.9 \times 10^{-3}(z^*)$	mm^4/Ns
$m(z^*)$	$3.0 + 5.0(z^*)$	–
D	(DT-MRI from Pierce et al., 2016)	–

two-step, optimization scheme (treating the simulations from Cases 1, 2, or 3 as a 'black box') used to determine the fitted parameters (k_1 and k_2) that best reproduce the experimentally determined stress-stretch response, see Fig. 4.

In the first step, we obtain a preliminary fitting from a surrogate model (Appendix B), and thereafter we apply a gradient-based method to determine the final fitting results. For the first step we use Latin Hypercube Sampling (LHS) (McKay et al., 1979) as our design of experiment (DoE) method to determine the locations of sample points within our design space and Kriging to interpolate between sample points (Oliver and Webster, 1990; Cressie, 1990).

In our two optimization schemes we calculate the root-mean-squared error (RMSE) at each experimental stretch, i.e. when $\lambda_{exp} = \lambda_{Ell}$, as

$$\bar{e}_s = \sqrt{\left(\sum_{i=1}^{N_{Ell}} [\sigma_{exp,i} - \sigma_{Ell,i}]^2 \right) / N_{exp}}, \tag{24}$$

where the subscript Ell refers to the experimental data of Elliott et al. (2002) and N_{Ell} is the total number of experimental data points therein.

To illustrate the different fitting results we plot Cauchy stress vs. experimentally determined stretch, and quantify the percent differences in the resulting material parameters using Case 1 as a benchmark.

2.4. Stress-relaxation test in unconfined compression

Next we model a stress-relaxation test of a full-thickness cuboid of cartilage (2 mm × 2 mm × 2.6 mm) in unconfined compression based on Diffusion Tensor MRI data detailed in Pierce et al. (2010). Our image-driven FE model consists of a 50 μm × 1 mm × 2.6 mm slice of the specimen meshed with 510 20-node hexahedral elements, see Fig. 7(a) Section 2.3. We fix nodes in dir-3 at minimum to zero displacement in all degrees-of-freedom (and $\mathbf{w}_{FS} = \mathbf{0}$). Next we fix nodes internal to the cartilage specimen in dir-1 and dir-2 with symmetry boundary conditions in their respective directions, i.e. plane-strain conditions. We then apply a linear displacement ramp to the articulating surface of the cuboid specimen (dir-3 equals maximum) at a rate of 2.6×10^{-3} mm/s until we reach an applied stretch of 0.9 (i.e. 10% compression) in 100 s, and then hold this displacement for another 700 s (relaxation). Nodes external to the cartilage specimen are free to expand or contract (and $p = 0$).

Table 2 summarizes the material parameters we use to model human patellar cartilage through the full thickness (Pierce et al., 2016), where the fixed charge density c_{0S}^{fc} is given as a piece-wise linear function (Räsänen et al., 2017). The remaining parameters come from Table 1. We apply the DT-MRI data from Pierce et al. (2010) to create an image-driven FE mesh and set **D** element-wise by application of the corresponding diffusion tensors. In this way the FE model reflects both

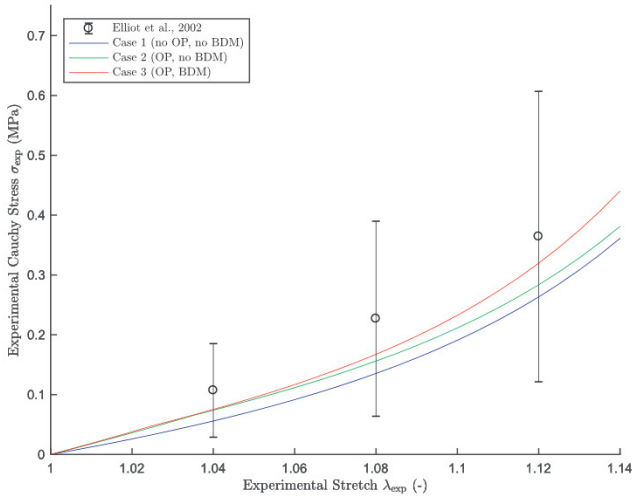

Fig. 5. Experimental Cauchy stress-stretch responses of Cases 1, 2, and 3 using $k_1 = 3.0$ MPa, $k_2 = 8.0$ (Pierce et al., 2013a). We include the experimental data (mean ± standard deviation) of Elliott et al. (2002) for context. Since we compare our results with experimental data, we present our results consistent with the experimentally determined values, cf. (22) and (23).

Table 3
Quantitative comparison of the Cauchy stress responses of Cases 1, 2, and 3 at the stretch values from the experiment (λ_{exp}) using $k_1 = 3.0$ MPa, $k_2 = 8.0$ (cf. Fig. 5).

	σ_{exp} (kPa)		
λ_{exp} (–)	Case 1	Case 2 (δ)	Case 3 (δ)
1.04	56.0	74.0 (+32.3%)	75.3 (+34.6%)
1.08	135.4	156.2 (+15.3%)	167.4 (+23.6%)
1.12	263.3	283.6 (+7.7%)	319.7 (+21.4%)
1.20	992.1	1009.1 (+1.7%)	1263.1 (+27.3%)

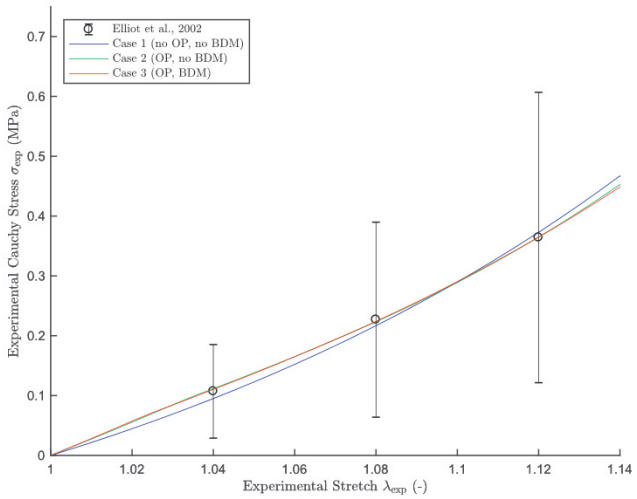

Fig. 6. Experimental Cauchy stress-experimental stretch responses of Cases 1, 2, and 3 for a global fitting (design space $k_1 \in [0, 10]$ (MPa), $k_2 \in (0, 15]$) to Elliott et al. (2002). We provide a zoomed-in illustration of the area highlighted by the dashed line, with inflection point at $\lambda_{exp} = 1.03$, in Appendix C.

the measured geometry and microstructure of the specimen.

We simulate the same stress-relaxation test using three methods (Cases 1, 2, and 3; Section 2.3.1). We compare the different bulk responses by plotting the global force-displacement response, and we quantify the percent differences in the results at 100 s (initial peak displacement) and 800 s (nearly fully relaxed) using Case 1 as a benchmark. To illustrate the different intra-tissue responses we plot distributions of axial cauchy stress and interstitial fluid pressure also at 100 and 800 s.

Table 4
Quantitative comparison of the Cauchy stress responses of Cases 1, 2, and 3 at the stretch values from the experiment (λ_{exp}) using best fit with $k_1 \in [0, 10]$ (MPa) and $k_2 \in (0, 15]$ as a global design space (cf. Fig. 6).

	σ_{exp} (kPa)		
λ_{exp} (–)	Case 1	Case 2 (δ)	Case 3 (δ)
1.04	95.1	111.5 (+ 17.3%)	110.4 (+ 16.2%)
1.08	216.8	223.4 (+ 3.1%)	224.1 (+ 3.4%)
1.12	372.9	364.9 (– 2.1%)	364.8 (– 2.2%)
1.20	838.4	820.1 (– 2.2%)	770.1 (– 8.2%)

Table 5
Fitted material (fiber) parameters k_1, k_2, RMSE error $\bar{e}_s$, and in parentheses the percent difference δ relative to Case 1 (no OP, no BDM) with $k_1 \in [0, 10]$ (MPa) and $k_2 \in (0, 15]$ as a global design space.

Results	Case 1	Case 2 (δ)	Case 3 (δ)
k_1 [MPa]	5.7	4.9 (– 13%)	4.9 (– 13%)
k_2 [-]	1.2	2.1 (+ 65%)	0.90 (– 27%)
$\bar{e}_s$ [MPa]	0.010	0.0033 (– 68%)	0.0025 (– 76%)

3. Results

We successfully implemented the mechanical effects of osmotic pressure (Karajan, 2009; Ehlers et al., 2009) into an existing constitutive model for cartilage (Pierce et al., 2016), and implemented the backward displacement method (extended from Bols et al., 2013) to determine the prestretched/prestressed states induced by osmotic loading in (imaged) initial configurations of the FE models.

3.1. Uniaxial extension test

3.1.1. Comparing simulation methods

Fig. 5 illustrates the experimental Cauchy stress-stretch responses of Cases 1, 2, and 3 using $k_1 = 3.0$ MPa, $k_2 = 8.0$ (Pierce et al., 2013a). In Fig. 5 we present the stretch results as those from the experiment (λ_{exp}), and the corresponding Cauchy stresses (σ_{exp}), cf. (22) and (23). Following the definition, the experimentally determined stretches and stresses always start from $[\sigma_{exp}, \lambda_{exp}] = [0, 1]$ in the imaged configuration. Finally, we compare the three cases quantitatively in Table 3.

3.1.2. Fitting model parameters

Using a global design space in conjunction with parameter fitting to the three different computational methods to simulate the uniaxial tension test (Cases 1, 2, and 3; Fig. 3), we obtain three distinct mechanical responses and three distinct parameter sets. Fig. 6 illustrates the experimental Cauchy stress-experimental stretch responses of Cases 1, 2, and 3 using $k_1 = 3.0$ MPa, $k_2 = 8.0$ (Pierce et al., 2013a) as an initial guess. In Fig. 6 we choose $k_1 \in [0, 10]$ (MPa) and $k_2 \in (0, 15]$ as a global design space. Somewhat unexpectedly, there is an inflection point at $\lambda_{exp} = 1.03$ and we provide a zoomed-in illustration of this in Appendix C. We compare the three cases quantitatively in Table 4. Table 5 provides the corresponding fitted material (fiber) parameters k_1, k_2 and RMSE error $\bar{e}_s$ relative to Case 1.

3.2. Stress-relaxation test in unconfined compression

Fig. 7(a) schematically illustrates the specimen used for the stress-relaxation test in unconfined compression. Fig. 7(b) illustrates the

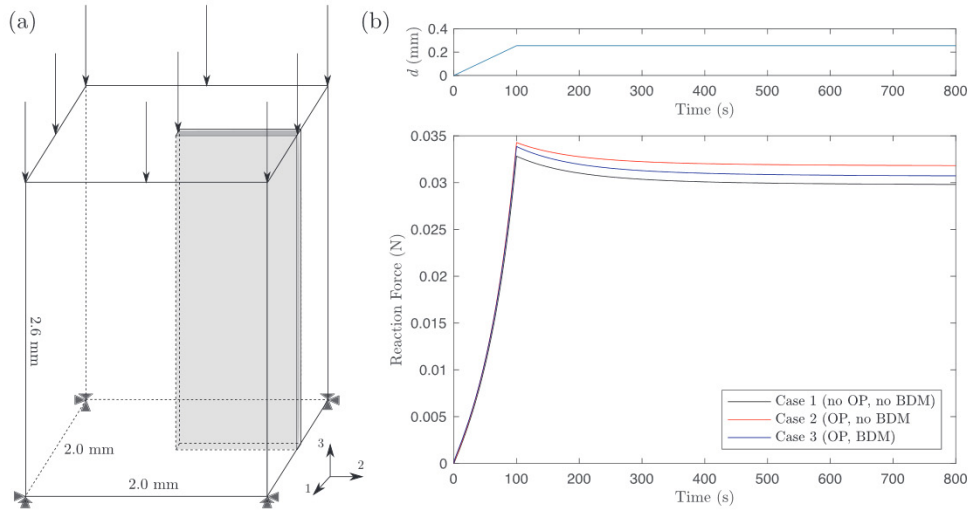

Fig. 7. (a) Schematic illustration of the specimen used for the stress-relaxation test in unconfined compression. (b) The displacement vs. time applied to the articulating surface of the specimen (top) and the resulting reaction force vs. time (bottom) for Cases 1, 2, and 3.

Table 6
Quantitative comparison of the reaction force responses of Cases 1, 2, and 3 at times 100 s (peak response) and 800 s (relaxed response).

	Reaction Force (N)		
Time (s)	Case 1	Case 2 (δ)	Case 3 (δ)
100	0.0328	0.0343 (+4.45%)	0.0339 (+3.17%)
800	0.0298	0.0318 (+6.74%)	0.0307 (+3.05%)

displacement vs. time applied to the articulating surface of the specimen (top) and the resulting reaction force vs. time (bottom) for Cases 1, 2, and 3. We compare the three cases quantitatively in Table 6.

Fig. 8 illustrates the distributions of axial cauchy stress and interstitial fluid pressure for Cases 1, 2, and 3 at times 100 s (peak response) and 800 s (relaxed response) (Table D1).

4. Discussion

We establish a new approach to image-driven FE simulations of cartilage. We first established a new constitutive model for articular cartilage by extending our recent model (Pierce et al., 2016) to include the mechanical effects of osmotic pressure following the approach detailed by Karajan (2009), Ehlers et al. (2009). We then overcame a theoretical inconsistency arising in image-driven FE simulations (the *in-vivo* imaged geometry used to construct the model is not an unloaded, stress-free reference configuration) by determining the osmotically loadedprestretched/prestressedstate within the solid matrix of the FE model using the backward displacement method following Bols et al. (2013). Starting from this state we may solve boundary value problems of interest.

To demonstrate the efficacy of our new approach we compare results from FE simulations assuming three cases: Case 1 (no OP, no BDM), Case 2 (OP, no BDM), and Case 3 (OP, BDM). To further demonstrate efficacy we fit material parameters related to the collagen fibers to experimental data, using the same three cases, and again compare results. Our new constitutive model, combined with our fitting and simulation workflow, can capture the mechanical effects of osmotic pressure within a theoretically consistent image-driven configuration.

In our representative test cases in Section 2.3 we assume that the parameters $n^{\mathrm{S}}_{0\mathrm{S}} = 0.21$ and $c^{\mathrm{fc}}_{0\mathrm{S}} = 2.0 \times 10^{-7}\,\mathrm{mol/mm^3}$ were determined in a stress-free reference configuration. During the Case 3 simulations (OP, BDM) the values of both $n^{\mathrm{S}}_{0\mathrm{S}}$ and $c^{\mathrm{fc}}_{0\mathrm{S}}$ change by $\approx 3-4\%$ in the osmotically loaded, imaged configuration, see Appendix D. Additionally, we assume that $k_{0\mathrm{S}} = 6.2 \times 10^{-3}\,\mathrm{mm^4/(N\,s)}$ was also determined in a stress-free reference configuration. The physical meaning of this parameter also changes if referenced to the osmotically loaded, imaged configuration via functional dependence on n^{F}, cf. (10). In practice, it's more likely to determine these parameters experimentally from the osmotically swollen state, i.e. $n^{\mathrm{S}}_{\mathrm{img\,S}}$, $c^{\mathrm{cf}}_{\mathrm{img\,S}}$, and $k_{\mathrm{img\,S}}$ versus $n^{\mathrm{S}}_{0\mathrm{S}}$, $c^{\mathrm{fc}}_{0\mathrm{S}}$, and $k_{0\mathrm{S}}$. In this case, for consistency, both $n^{\mathrm{S}}_{0\mathrm{S}}$ and $c^{\mathrm{fc}}_{0\mathrm{S}}$ should be determined via fitting within the inverse problem, and $k_{\mathrm{img\,S}}$ should be checked for correct implementation in the imaged configuration.

4.1. Uniaxial extension test

4.1.1. Comparing simulation methods

Importantly, in Case 3 (OP, BDM) we recover the imaged configuration with a prestressed state in equilibrium with the (assumed) known osmotic load. Cases 1, 2, and 3 (Fig. 3) lead to distinctly different predictions for stresses at the same stretches, cf. Fig. 5, clearly demonstrating the importance of considering the osmotically loading, prestressed configuration in order to better interpret the experimental results. Given fixed parameters k_1 and k_2, Case 3 shows the stiffest behavior. This is largely because the collagen fibers are pre-tensioned (prestressed), starting from the imaged configuration and thus their contribution to the total stress is greater.

4.1.2. Fitting model parameters

Case 3, which includes the effects of prestress/prestretch due to osmotic loading in the imaged configuration, is theoretically consistent with most laboratory experiments and thus we consider it the most realistic. With both the osmotic pressure and the correct prestressed configuration included, our Case 3 simulations determined lower k_1 and k_2, as well as smaller RMSE errors, under the same global fitting and with respect to cases 1 and 2. This agrees with our expectations based on the discussion in Section 4.1.1. Note that the original experimental data from cartilage in the middle zone does behave nearly linearly within the applied range of stretches (Elliott et al., 2002). With less nonlinear behaviors, the different cases have smaller differences in predicted stresses (to better illustrate the effects we provided quantitative data to $\lambda_{\mathrm{exp}} = 1.20$). However, cartilage can show highly nonlinear behavior, especially in the superficial zone where collagen fibers often align to create a strongly anisotropic tissue (Kempson et al., 1973; Elliott et al., 2002; Huang et al., 2005). Our model, proposed here, can fit such nonlinear and anisotropic responses.

Modeling the prestretched/prestressed condition not only influences the values of the fitted material parameters, but also creates a slight

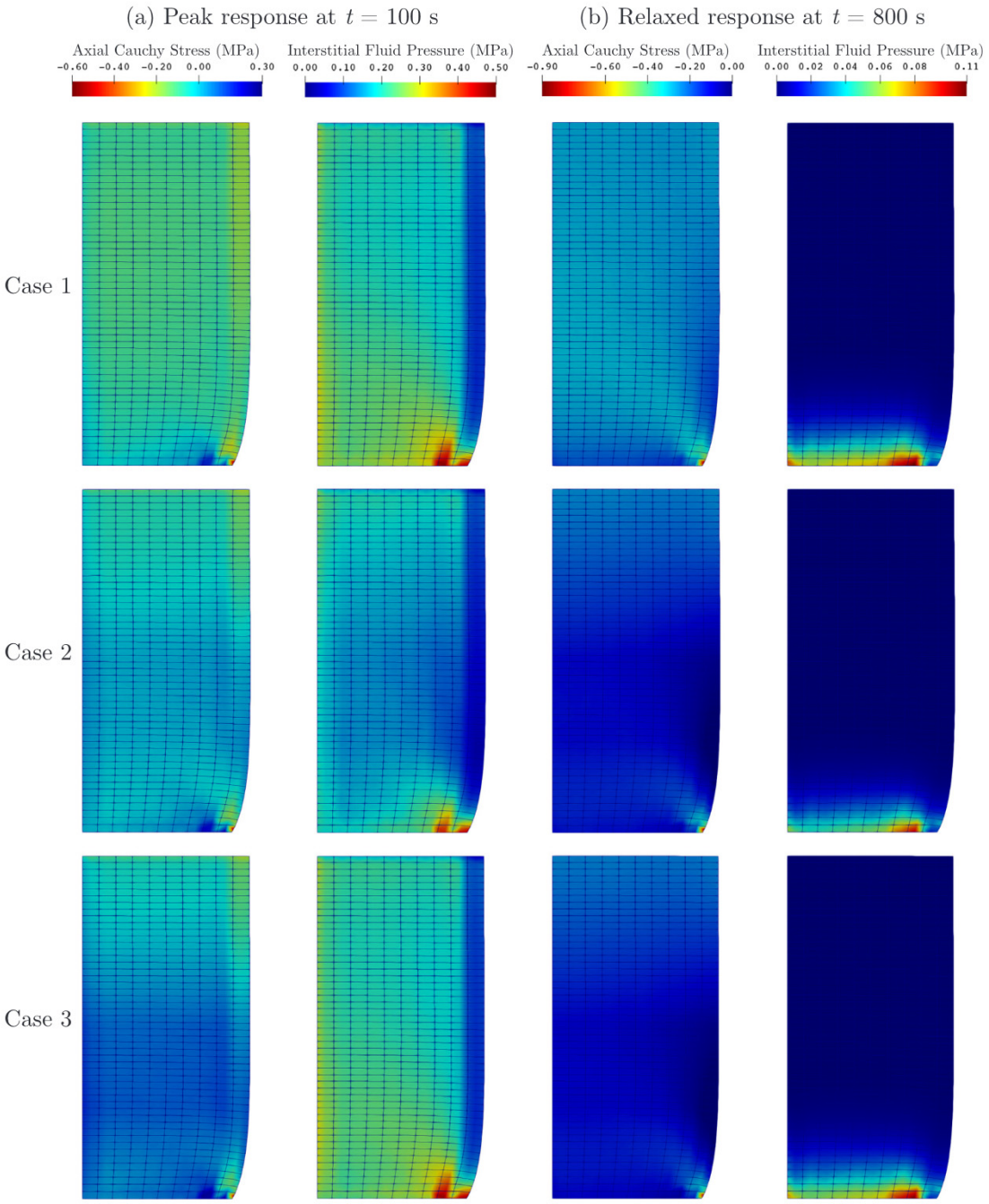

Fig. 8. (a) Peak and (b) relaxed responses, at times 100 s and 800 s respectively (columns), shown as distributions of axial Cauchy stress and interstitial fluid pressure for Cases 1, 2, and 3 (rows).

inflection point in the overall stress-stretch behavior predicted in the uniaxial tensile test. Overall, as the loaded direction is stretched in the uniaxial tensile test, the remaining two (unconstrained) directions tend to shrink due to incompressibility. During the uniaxial tension test, these two unconstrained directions first contract to the at-rest-length (of the fibers) and then go into compression (Bursać et al., 2000). While passing the at-rest-length, fibers aligned in these directions switch from tension (load-bearing) to compression (non-load-bearing) and no longer contribute to the total stress state, cf. (9). This change from tension to compression creates a slight inflection point in the overall stress-stretch behavior seen at $\lambda_{exp} = 1.03$ in Fig. C1 (zoomed in from Fig. 6(b)).

4.2. Stress-relaxation test in unconfined compression

Cases 1, 2, and 3 show virtually identical bulk force-displacement responses during initial loading, and these are nonlinear (Fig. 7(b) and Table 6). However, Case 2 reaches the highest peak force since the displacement loading and osmotic loading occur simultaneously from a stress-free reference configuration. Case 1, which neglects osmotic swelling, shows the lowest peak force of the three cases. In comparison, Case 3 starts from the same reference geometry, but in an equilibrium state where the fibers are pre-tensioned due to the osmotic swelling. This prestressed/prestrained state results in an intermediate peak force and a slightly faster relaxation. Finally, the total bulk relaxation of the specimen is less than might be expected. This is likely due to the relatively slow loading, the large free-draining surface area relative to the

total volume, and fact that viscoelasticity of the solid constituents is neglected in the example, i.e. $\beta_\alpha = 0$, $\tau_\alpha = 0.1$, $\alpha \in \{\text{IM, FN}\}$.

Cases 1, 2, and 3 show distinctly different distributions of axial Cauchy stress, particulary at peak response (100 s), cf. Fig. 8. Case 1 starts from a stress-free distribution but at 100 s shows a largely negative Cauchy stress through the thickness due to the compression. Case 2 starts similarly but the Cauchy stress remains near zero through the thickness due to osmotic pressure countering the compression. Conversely, Case 3 starts from an overall positive axial stress distribution prior to compression. At 100 s the applied compression generates a near-zero axial stress in the superficial zone while stresses in the middle and deep zones remain positive. After relaxation (at 800 s), Case 1 remains in compression through the thickness while cases 2 and 3 are very similar and nearly zero demonstrating a balance between compression and osmotic swelling.

Cases 1 and 3 show very similar distributions in interstitial fluid pressure at peak response while this is generally lower in Case 2. Note that both Case 1 and Case 3 start in equilibrium, i.e. zero interstitial fluid pressure, and with the same geometry. After relaxation the distributions in interstitial fluid pressure for all three cases are nearly zero, and only a small pressure remains in the deep zone of the specimen (i.e. not fully relaxed).

4.3. Limitations and opportunities

It is important to note that our new constitutive model and modeling methods capture only the mechanical effects of Donnan osmotic pressure based on the simplifying assumption of Lanir (1987). Other contributions to the swelling pressure include charge-charge repulsion. Triphasic or quadri-phasic constitutive models seek to capture other mechanical-electrochemical coupling effects generated from the existence of ions and fixed charges, such as streaming potential and electroosmosis, e.g. van Loon et al. (2003), Ateshian et al. (2011). These cartilage models capture more physics, but such fidelity is more computationally expensive and is not always relevant.

In our new method, we determine the osmotically prestretched/prestressed state within the cartilage in equilibrium with the (imaged) initial configuration of the FE model using the backward displacement method (Bols et al., 2013) prior to solving boundary value problems of interest. This equilibrium condition could be similarly determined by application of other computational approaches, e.g. Grytz and Downs (2013), Weisbecker et al. (2014), Maas et al. (2016), and where the latter is implemented as a plugin in FEBio.

Our results highlight the importance of determining the prestretched/prestressed state within the solid matrix induced by osmotic loading in the (imaged) initial configuration prior to solving boundary value problems of interest. With our new constitutive model and modeling methods, we hope to improve the fidelity of FE-based, patient-specific biomechanical simulations of joints and cartilage. “Open Knee(s): Virtual Biomechanical Representations of the Knee Joint” (Erdemir, 2016) offers free access to hexahedral meshes of specific patients. Similarly, we offer free access to hexahedral meshes of eight patients from the OAI database (Rodriguez-Vila et al., 2017) and a MATLAB implementation of our meshing software, both free for download at im.engr.uconn.edu/downloads.php. Improved simulations can provide medical researchers with new information often unavailable in a clinical setting, information that may contribute to better insight into the pathophysiology of cartilage diseases. With our new fitting methods, we also hope to better fit available experimental data.

Acknowledgements

We gratefully acknowledge funding from the National Science Foundation CAREER 1653358. We also thank José Raya and Christian Glaser from the NYU Langone Medical Center for use of the diffusion tensor magnetic resonance imaging data.

Conflicts of interest

We have no conflicts of interest to report.

Appendix A

In articular cartilage, we determine the osmotic pressure from Donnan equilibrium as (Karajan, 2009)

$$\Delta\pi = R\Theta\left[\sqrt{4(\bar{c}_\mathrm{m})^2 + (c_\mathrm{m}^\mathrm{fc})^2} - 2\bar{c}_\mathrm{m}\right], \tag{25}$$

where $\bar{c}_\mathrm{m}$ is the ion concentration of the external solution, and c_m^fc is the concentration of the fixed charges. Starting from the osmotic contribution to the solid stress of the model (Section 2.1), we compute the second Piola-Kirchhoff stress as

$$\begin{aligned}
\mathbf{S}_\mathrm{OP}^\mathrm{S} &= 2\frac{\partial\Psi_\mathrm{OP}^\mathrm{S}}{\partial\mathbf{C}_\mathrm{S}} \\
&= 2\frac{\partial\Psi_\mathrm{OP}^\mathrm{S}}{\partial c_\mathrm{m}^\mathrm{fc}}\frac{\partial c_\mathrm{m}^\mathrm{fc}}{\partial\det\mathbf{F}_\mathrm{S}}\frac{\partial\det\mathbf{F}_\mathrm{S}}{\partial\det\mathbf{C}_\mathrm{S}}\frac{\partial\det\mathbf{C}_\mathrm{S}}{\partial\mathbf{C}_\mathrm{S}} \\
&= \det\mathbf{F}_\mathrm{S}\frac{\partial\Psi_\mathrm{OP}^\mathrm{S}}{\partial c_\mathrm{m}^\mathrm{fc}}\frac{\partial c_\mathrm{m}^\mathrm{fc}}{\partial\det\mathbf{F}_\mathrm{S}}\mathbf{C}_\mathrm{S}^{-1} \\
&= -\det\mathbf{F}_\mathrm{S}R\Theta\left[\sqrt{4(\bar{c}_\mathrm{m})^2 + (c_\mathrm{m}^\mathrm{fc})^2} - 2\bar{c}_\mathrm{m}\right]\mathbf{C}_\mathrm{S}^{-1} \\
&= -\det\mathbf{F}_\mathrm{S}\Delta\pi\mathbf{C}_\mathrm{S}^{-1}.
\end{aligned} \tag{26}$$

We then compute the Cauchy stress as

$$\boldsymbol{\sigma}_\mathrm{OP}^\mathrm{S} = \det\mathbf{F}_\mathrm{S}^{-1}\mathbf{F}_\mathrm{S}\mathbf{S}_\mathrm{OP}^\mathrm{S}\mathbf{F}_\mathrm{S}^\mathrm{T} = -\Delta\pi\mathbf{I}. \tag{27}$$

Appendix B

By running the FE simulation S, we observe y at n sites (determined by DoE)

$$\mathbf{S} = [\mathbf{x}^{(1)},\ldots,\mathbf{x}^{(n)}]^\mathrm{T} \in \mathbb{R}^{n\times m},\ \mathbf{x} = \{x_1,\ \ldots,x_m\} \in \mathbb{R}^m, \tag{28}$$

with the corresponding responses

$$\mathbf{y}_s = [y^{(1)},...,y^{(n)}]^{\mathrm{T}} = [y(\mathbf{x}^{(1)}),...,y(\mathbf{x}^{(n)})]^{\mathrm{T}} \in \mathbb{R}^n. \tag{29}$$

The pair $(\mathbf{S}, \mathbf{y}_s)$ is thus the sampled data in vector space. Kriging, an interpolating method, includes the observed data at all sample points and provides a statistic prediction of an unknown function by minimizing its mean-squared-error (MSE). With Kriging, we the treat outputs of our (deterministic) FE simulations as realizations of a random function (or stochastic process), defined as the sum of a global trend function $\mathbf{f}^{\mathrm{T}}(\mathbf{x})\boldsymbol{\beta}$ and a Gaussian random function $Z(\mathbf{x})$ as

$$y(\mathbf{x}) = \mathbf{f}^{\mathrm{T}}(\mathbf{x})\boldsymbol{\beta} + Z(\mathbf{x}), \tag{30}$$

where we define $\mathbf{f}(\mathbf{x}) = [f_0(\mathbf{x}),...,f_{p-1}(\mathbf{x})]^{\mathrm{T}} \in \mathbb{R}^p$ with a set of the regression basis functions, $\boldsymbol{\beta} = [\beta_0,...,\beta_{p-1}]^{\mathrm{T}} \in \mathbb{R}^p$ denotes the vector of the corresponding coefficients, and we take $\mathbf{f}^{\mathrm{T}}(\mathbf{x})\boldsymbol{\beta}$ as a constant β_0. In (30), $Z(\mathbf{x})$ denotes a stationary random process with zero mean, variance σ^2, and nonzero covariance

$$\mathrm{Cov}[Z(\mathbf{x}), Z(\mathbf{x}')] = \sigma^2 R(\mathbf{x}, \mathbf{x}'), \tag{31}$$

where $R(\mathbf{x}, \mathbf{x}')$ is the correlation function only dependent on the Euclidean distance between any two sites $\mathbf{x}$ and $\mathbf{x}'$ in the design space (McKay et al., 1979). We adopt a Gaussian exponential correlation function

$$R(\mathbf{x}, \mathbf{x}') = \exp\left[-\sum_{k=1}^{m} \theta_k |x_k - x'_k|^{p_k}\right], \ 1 < p_k \leq 2, \tag{32}$$

where $[\theta_1, \theta_2,..., \theta_m]^{\mathrm{T}}$ and $\boldsymbol{p} = [p_1, p_2,..., p_m]^{\mathrm{T}}$ denote the vectors of unknown model parameters (hyper parameters) to be determined.

We write the Kriging predictor $\hat{y}(\mathbf{x})$ for any untried $\mathbf{x}$ as

$$\hat{y}(\mathbf{x}) = \beta_0 + \mathbf{r}^{\mathrm{T}}(\mathbf{x})\mathbf{R}^{-1}(\mathbf{y}_s - \beta_0\mathbf{1}), \tag{33}$$

where $\mathbf{1} \in \mathbb{R}^n$ is a vector of ones and the generalized least-square estimation of β_0 is

$$\beta_0 = (\mathbf{1}^{\mathrm{T}}\mathbf{R}^{-1}\mathbf{1})^{-1}\mathbf{1}^{\mathrm{T}}\mathbf{R}^{-1}\mathbf{y}_s. \tag{34}$$

We define $\mathbf{R}$ and $\mathbf{r}$, the correlation matrix and correlation vector respectively, as

$$\mathbf{R} = \begin{bmatrix} R(\mathbf{x}^{(1)}, \mathbf{x}^{(1)}) & R(\mathbf{x}^{(1)}, \mathbf{x}^{(2)}) & \cdots & R(\mathbf{x}^{(1)}, \mathbf{x}^{(n)}) \\ R(\mathbf{x}^{(2)}, \mathbf{x}^{(1)}) & R(\mathbf{x}^{(2)}, \mathbf{x}^{(2)}) & \cdots & R(\mathbf{x}^{(2)}, \mathbf{x}^{(n)}) \\ \vdots & \vdots & \ddots & \vdots \\ R(\mathbf{x}^{(n)}, \mathbf{x}^{(1)}) & R(\mathbf{x}^{(n)}, \mathbf{x}^{(2)}) & \cdots & R(\mathbf{x}^{(n)}, \mathbf{x}^{(n)}) \end{bmatrix} \in \mathbb{R}^{n\times n}, \tag{35}$$

$$\mathbf{r} = \begin{bmatrix} R(\mathbf{x}^{(1)}, \mathbf{x}) \\ R(\mathbf{x}^{(2)}, \mathbf{x}) \\ \vdots \\ R(\mathbf{x}^{(n)}, \mathbf{x}) \end{bmatrix} \in \mathbb{R}^n, \tag{36}$$

where $R(\mathbf{x}^{(i)}, \mathbf{x}^{(j)})$ denotes the correlation between any two observed points $\mathbf{x}^{(i)}$ and $\mathbf{x}^{(j)}$, $R(\mathbf{x}^{(i)}, \mathbf{x})$ denotes the correlation between the ith observed point $\mathbf{x}^{(i)}$ and the untried point $\mathbf{x}$.

The Kriging model provides an uncertainty estimation (or MSE) for each prediction

$$\hat{s}^2 = \sigma^2[1 - \mathbf{r}^{\mathrm{T}}\mathbf{R}^{-1}\mathbf{r} + (\mathbf{r}^{\mathrm{T}}\mathbf{R}^{-1}\mathbf{1} - 1)^2]/(\mathbf{1}^{\mathrm{T}}\mathbf{R}^{-1}\mathbf{1}), \tag{37}$$

which is very useful for refinement of sample points. Assuming that the sampled data are distributed according to a Gaussian process, we consider the responses at sampling sites as correlated random functions with the corresponding likelihood function

$$L(\beta_0, \sigma^2, \theta, \mathbf{p}) = \frac{1}{\sqrt{2\pi(\sigma^2)^n|\mathbf{R}|}} \exp\left(-\frac{1}{2}\frac{(\mathbf{y}_s - \beta_0\mathbf{1})^{\mathrm{T}}\mathbf{R}^{-1}(\mathbf{y}_s - \beta_0\mathbf{1})}{\sigma^2}\right). \tag{38}$$

We obtain the optimal estimation of β_0

$$\beta_0(\theta, \mathbf{p}) = (\mathbf{1}^{\mathrm{T}}\mathbf{R}^{-1}\mathbf{1})^{-1}\mathbf{1}^{\mathrm{T}}\mathbf{R}^{-1}\mathbf{y}_s, \tag{39}$$

and the process variance σ^2

$$\sigma^2(\beta_0, \theta, \mathbf{p}) = \frac{1}{n}(\mathbf{y}_s - \beta_0\mathbf{1})^{\mathrm{T}}\mathbf{R}^{-1}(\mathbf{y}_s - \beta_0\mathbf{1}), \tag{40}$$

analytically, but they still depend on the remaining hyper-parameters $\theta = [\theta_1, \theta_2,..., \theta_m]^{\mathrm{T}}$ and $\mathbf{p} = [p_1, p_2,..., p_m]^{\mathrm{T}}$. Substituting these into the associated likelihood function (38) and taking the logarithm, we maximize

$$MLE(\theta, \mathbf{p}) = -n \ln \sigma^2(\theta, \mathbf{p}) - \ln |\mathbf{R}(\theta, \mathbf{p})|, \tag{41}$$

using a numerical optimization algorithm, e.g. gradient-based optimization (Han and Zhang, 2012).

Appendix C

See Fig. C1.

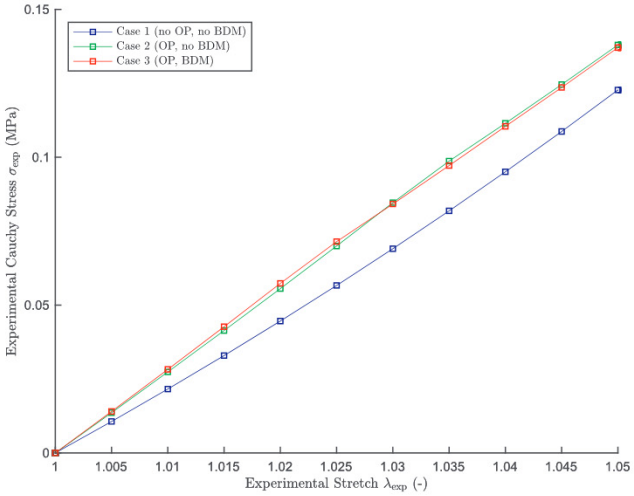

Fig. C1. Experimental Cauchy stress-stretch responses of Cases 1, 2, and 3 for global fitting $k_1 \in [0, 10]$ (MPa), $k_2 \in [0, 15]$ zoomed-in to highlight the inflection point at $\lambda_{exp} = 1.03$. This is the area highlighted by the dashed line in Fig. 6(b).

Appendix D

See Table D1.

Table D1
Change in the material parameters (solid volume fraction and fixed charge density) for Case 3 (OP, BDM) simulations, from the stress-free reference configuration (n^{S}_{0S} and c^{fc}_{0S}) to the osmotically loaded, imaged configuration ($n^{S}_{img\,S}$ and $c^{cf}_{img\,S}$), and in parentheses the percent difference δ relative to the stress-free reference.

Case 3 (k_1, k_2)	n^{S}_{0S} [-]	$n^{S}_{img\,S}$ [-] (δ)	c^{fc}_{0S} [mol/mm ^{3}]	$c^{cf}_{img\,S}$ [mol/mm^3] (δ)
Pierce et al. (2013a)	0.2138	0.2070 (− 3.18%)	2.000×10^{-7}	1.920×10^{-7} (− 4.01%)
Parameter Fitting	0.2138	0.2077 (− 2.84%)	2.000×10^{-7}	1.928×10^{-7} (− 3.58%)

References

Abdullah, O.M., Othman, S.F., Zhou, X.J., Magin, R.L., 2007. Diffusion tensor imaging as an early marker for osteoarthritis. Proc. Int. Soc. Magn. Reson. Med. 15, 814.

Ateshian, G.A., Albro, M.B., Maas, S., Weiss, J.A., 2011. Finite element implementation of mechanochemical phenomena in neutral deformable porous media under finite deformation. J. Biomech. Eng. 133, 081005 (12 pages).

Ateshian, G.A., Rajan, V., Chahine, N.O., Canal, C.E., Hung, C.T., 2009. Modeling the matrix of articular cartilage using a continuous fiber angular distribution predicts many observed phenomena. J. Biomech. Eng. 131, 61003.

Bingham, J.T., Papannagari, R., Van de Velde, S.K., Gross, C., Gill, T.J., Felson, D.T., Rubash, H.E., Li, G., 2008. In vivo cartilage contact deformation in the healthy human tibiofemoral joint. Rheumatology 47, 1622–1627.

Bishop, A.W., 1959. The principle of effective stress. Tek. Ukebl. 39, 859–863.

Bluhm, J., 2002. Modelling of saturated thermo-elastic porous solids with different phase temperatures. In: Ehlers, W., Bluhm, J. (Eds.), Porous Media: Theory, Experiments and Numerical Applications. Springer-Verlag, Berlin, Heidelberg, New York, pp. 87–120.

Bols, J., Degroote, J., Trachet, B., Verhegghe, B., Segers, P., Vierendeels, J., 2013. A computational method to assess the in vivo stresses and unloaded configuration of patient-specific blood vessels. J. Comput. Appl. Math. 246, 10–17.

Bowen, R.M., 1980. Incompressible porous media models by use of theory of mixtures. Int. J. Eng. Sci. 18, 1129–1148.

Bowen, R.M., 1982. Compressible porous media models by use of the theory of mixtures. Int. J. Eng. Sci. 20, 697–735.

Broom, N.D., Marra, D.L., 1986. Ultrastructural evidence for fibril-to-fibril associations in articular cartilage and their functional implication. J. Anat. 146, 185–200.

Bursać, P., McGrath, C.V., Eisenberg, S.R., Stamenović, D., 2000. A microstructural model of elastostatic properties of articular cartilage in confined compression. J. Biomech. Eng. 122, 347–353.

Chahine, N.O., Chen, F.H., Hung, C.T., Ateshian, G.A., 2005. Direct measurement of osmotic pressure of glycosaminoglycan solutions by membrane osmometry at room temperature. Biophys. J. 89, 1543–1550.

Chan, D.D., Cai, L., Butz, K.D., Trippel, S.B., Nauman, E.A., Neu, C.P., 2016. In vivo articular cartilage deformation: noninvasive quantification of intratissue strain during joint contact in the human knee. Sci. Rep. 6, 19220.

Chen, Y., Chen, X., Hisada, T., 2006. Non-linear finite element analysis of mechanical electrochemical phenomena in hydrated soft tissues based on triphasic theory. Int. J. Numer. Methods Eng. 65, 147–173.

Crema, M.D., Roemer, F.W., Marra, M.D., Burstein, D., Gold, G.E., Eckstein, F., Baum, T., Mosher, T.J., Carrino, J.A., Guermazi, A., 2011. Articular cartilage in the knee: current mr imaging techniques and applications in clinical practice and research. Radiographics 31, 37–61.

Cressie, N., 1990. The origins of kriging. Math. Geol. 22, 239–252.

de Boer, R., 2000. Theory of Porous Media. Highlights in the Historical Development and Current State. Springer-Verlag, Heidelberg.

de Visser, S.K., Bowden, J.C., Wentrup-Bryne, E., Rintoul, L., Bostrom, T., Pope, J.M., Momot, K.I., 2008a. Anisotropy of collagen fibre alignment in bovine cartilage: comparison of polarised light microscopy and spatially resolved diffusion-tensor measurements. Osteoarthr. Cartil. 16, 689–697.

de Visser, S.K., Crawford, R.W., Pope, J.M., 2008b. Structural adaptations in compressed articular cartilage measured by diffusion tensor imaging. Osteoarthr. Cartil. 16, 83–89.

Ehlers, W., 1989. Poröse medien - ein kontinuumsmechanisches Modell auf der Basis der Mischungstheorie. Ph.D. Thesis, Universität GH Essen, forschungsbericht aus dem Fachbereich Bauwesen 47.

Ehlers, W., 1993. Constitutive equations for granular materials in geomechanical context. In: Hutter, K. (Ed.), Continuum Mechanics in Environmental Sciences and Geophysics. Springer-Verlag, Wien, pp. 313–402, CISM Courses and Lectures no. 337.

Ehlers, W., Acartürk, A., Karajan, N., 2010. Advances in modelling saturated soft biological tissues and chemically active gels. Arch. Appl. Mech. 80, 467–478.

Ehlers, W., Karajan, N., Markert, B., 2009. An extended biphasic model for charged hydrated tissues with application to the intervertebral disc. Biomech. Model.

Mechanobiol. 8, 233–251.
Eipper, G., 1998. Theorie und Numerik finiter elastischer Deformationen in fluidgesättigten porösen Festkörpern. Ph.D. Thesis, Universität Stuttgart, bericht Nr. II-1 aus dem Institut für Mechanik (Bauwesen).
Elliott, D.M., Narmoneva, D.A., Setton, L.A., 2002. Direct measurement of the Poisson's ratio of human patella cartilage in tension. J. Biomech. Eng. 124, 223–228.
Erdemir, A., 2016. Open knee: open source modeling & simulation to enable scientific discovery and clinical care in knee biomechanics. J. Knee Surg. 29, 107–116.
Filidoro, L., Dietrich, O., Weber, J., Rauch, E., Oether, T., Wick, M., Reiser, M.F., Glaser, C., 2005. High-resolution diffusion tensor imaging of human patellar cartilage: feasibility and preliminary findings. Magn. Reson. Med. 53, 993–998.
Grytz, R., Downs, J.C., 2013. A forward incremental prestressing method with application to inverse parameter estimations and eye-specific simulations of posterior scleral shells. Comput. Methods Biomech. Biomed. Engin. 16, 768–780.
Han, Z.-H., Zhang, K.-S., 2012. Surrogate-based optimization. In: Real-World Applications of Genetic Algorithms. InTech, pp. 343–362.
Holzapfel, G.A., Gasser, T.C., Ogden, R.W., 2000. A new constitutive framework for arterial wall mechanics and a comparative study of material models. J. Elast. 61, 1–48.
Huang, C.-Y., Stankiewicz, A., Ateshian, G.A., Mow, V.C., 2005. Anisotropy, inhomogeneity, and tension-compression nonlinearity of human glenohumeral cartilage in finite deformation. J. Biomech. 38, 799–809.
Karajan, N., 2009. An extended biphasic description of the inhomogeneous and anisotropic intervertebral disc. Ph.D. Thesis, Stuttgart University.
Kempson, G.E., Muir, H., Pollard, C., Tuke, M., 1973. The tensile properties of the cartilage of human femoral condyles related to the content of collagen and glycosaminoglycans. Biochim. Biophys. Acta 297, 456–472.
Klika, V., Gaffney, E.A., Chen, Y.-C., Brown, C.P., 2016. An overview of multiphase cartilage mechanical modelling and its role in understanding function and pathology. J. Mech. Behav. Biomed. Mat. 62, 139–157.
Lanir, Y., 1987. Biorheology and flux in swelling tissue. I Biocomponent theory for small deformation including concentration effect. Biorheology 24, 173–187.
Lei, F., Szeri, A.Z., 2006. The influence of fibril organization on the mechanical behaviour of articular cartilage. Proc. R. Soc. Lond. A 462, 3301–3322.
Liu, F., Kozanek, M., Hosseini, A., de Velde, S.K.V., Gill, T.J., Rubash, H.E., Li, G., 2010. In vivo tibiofemoral cartilage deformation during the stance phase of gait. J. Biomech. 43, 658–665.
Maas, S.A., Erdemir, A., Halloran, J.P., Weiss, J.A., 2016. A general framework for application of prestrain to computational models of biological materials. J. Mech. Behav. Biomed. Mat. 61, 499–510.
Mansour, J.M., 2008. Biomechanics of cartilage. In: Oatis, C. A. (Ed.), Kinesiology: The Mechanics and Pathomechanics of Human Movement, 2nd edition, 2nd Edition. Lippincott Williams and Wilkins, Philadelphia, pp. 69–83.
van Loon, R., Huyghe, J., Wijlaars, M., Baaijens, F., 2003. 3d fe implementation of an incompressible quadriphasic mixture model. Int. J. Numer. Methods Eng. 57, 1243–1258.
McKay, M.D., Beckman, R.J., Conover, W.J., 1979. Comparison of three methods for selecting values of input variables in the analysis of output from a computer code. Technometrics 21, 239–245.
Meder, R., de Visser, S.K., Bowden, J.C., Bostrom, T., Pope, J.M., 2006. Diffusion tensor imaging of articular cartilage as a measure of tissue microstructure. Osteoarthr. Cartil. 14, 875–881.
Miehe, C., Göktepe, S., Lulei, F., 2004. A micro-macro approach to rubber-like materials - Part I: the non-affine micro-sphere model of rubber elasticity. J. Mech. Phys. Solids 52, 2617–2660.
Mow, V.C., Gu, W.Y., Chen, F.H., 2005. Structure and function of articular cartilage and meniscus. In: Mow, V.C., Huiskes, R. (Eds.), Basic Orthopaedic Biomechanics & Mechano-Biology. Lippincott Williams & Wilkins, Philadelphia, pp. 181–258, 3rd edition.
Oliver, M.A., Webster, R., 1990. Kriging: a method of interpolation for geographical information systems. Int. J. Geogr. Inf. Sci. 4, 313–332.
Park, S., Krishnan, R., Nicoll, S.B., Ateshian, G.A., 2003. Cartilage interstitial fluid load support in unconfined compression. J. Biomech. 36, 1785–1796.
Pence, T.J., 2012. On the formulation of boundary value problems with the incompressible constituents constraint in finite deformation poroelasticity. Math. Method Appl. Sci. 35, 1756–1783.
Pierce, D.M., Ricken, T., Holzapfel, G.A., 2013a. A hyperelastic biphasic fiber-reinforced model of articular cartilage considering distributed collagen fiber orientations: continuum basis, computational aspects and applications. Comput. Methods Biomech. Biomed. Eng. 16, 1344–1361.
Pierce, D.M., Ricken, T., Holzapfel, G.A., 2013b. Modeling sample/patient-specific structural and diffusional response of cartilage using DT-MRI. Int. J. Numer. Methods Biomed. Eng. 29, 807–821.
Pierce, D.M., Ricken, T., Neu, C.P., 2018. Image-driven constitutive modeling for fe-based simulation of soft tissue biomechanics. In: Cerrolaza, M., Shefelbine, S., Garzón-Alvarado, D. (Eds.), Numerical Methods and Advanced Simulation in Biomechanics and Biological Processes. Elsevier, Cambridge, MA, pp. 55–76.
Pierce, D.M., Trobin, W., Raya, J.G., Trattnig, S., Bischof, H., Glaser, C., Holzapfel, G.A., 2010. DT-MRI based computation of collagen fiber deformation in human articular cartilage: a feasibility study. Ann. Biomed. Eng. 38, 2447–2463.
Pierce, D.M., Unterberger, M.J., Trobin, W., Ricken, T., Holzapfel, G.A., 2016. A microstructurally based continuum model of cartilage viscoelasticity and permeability incorporating statistical fiber orientation. Biomech. Model. Mechanobiol. 15, 229–244.
Räsänen, L.P., Tanska, P., Zby`ň, Š., van Donkelaar, C.C., Trattnig, S., Nieminen, M.T., Korhonen, R.K., 2017. The effect of fixed charge density and cartilage swelling on mechanics of knee joint cartilage during simulated gait. J. Biomech. 61, 34–44.
Ricken, T., Bluhm, J., 2010. Remodeling and growth of living tissue: a multiphase theory. Arch. Appl. Mech. 80, 453–465.
Rodriguez-Vila, B., Sánchez-González, P., Oropesa, I., Gomez, E.J., Pierce, D.M., 2017. Automated hexahedral meshing of knee cartilage structures - application to data from the osteoarthritis initiative. Comput. Methods Biomech. Biomed. Engin. 20, 1543–1553.
Schroeder, Y., Wilson, W., Huyghe, J.M., Baaijens, F.P.T., 2006. Osmoviscoelastic finite element model of the intervertebral disc. Eur. Spine J. 15, 361–371.
Setton, L.A., Tohyama, H., Mow, V.C., 1998. Swelling and curling behaviors of articular cartilage. J. Biomech. Eng. 120, 355–361.
Simo, J.C., Pister, K.S., 1984. Remarks on rate constitutive equations for finite deformation problems: computational implications. Comput. Meth. Appl. Mech. Eng. 46, 201–215.
Skempton, A.W., 1960. Terzaghi's discovery of effective stress. In: Bjerrum, L., Casagrande, A., Peck, R.B., Skempton, A.W. (Eds.), From Theory to Practice in Soil Mechanics. John Wiley, New York, London, pp. 42–53.
Urban, J.P.G., Maroudas, A., 1981. Swelling of the intervertebral disc in vivo. Connect. Tissue Res. 9, 1–10.
Weisbecker, H., Pierce, D.M., Holzapfel, G.A., 2014. A generalized prestressing algorithm for finite element simulation of pre-loaded geometries with application to the aorta. Int. J. Numer. Methods Biomed. Eng. 30, 857–872.
Wilson, W., van Donkelaar, C.C., Huyghe, J.M., 2005. A comparison between mechano-electrochemical and biphasic swelling theories for soft hydrated tissues. J. Biomech. Eng. 127, 158–165.
Zhu, W.B., Mow, V.C., Koob, T.J., Eyre, D.R., 1993. Viscoelastic shear properties of articular cartilage and the effects of glycosidase treatments. J. Orthop. Res. 11, 771–781.